JACS
JOURNAL OF THE AMERICAN CHEMICAL SOCIETY

ARTICLE

pubs.acs.org/JACS

Surface-Directed Molecular Assembly of Pentacene on Monolayer Graphene for High-Performance Organic Transistors

Wi Hyoung Lee,[†,‡,∥] Jaesung Park,[‡,∥] Sung Hyun Sim,[§] Soojin Lim,[†] Kwang S. Kim,[*,‡] Byung Hee Hong,[*,§] and Kilwon Cho[*,†]

[†]Department of Chemical Engineering, Pohang University of Science and Technology, Pohang 790-784, Korea

[‡]Center for Superfunctional Materials, Department of Chemistry, Pohang University of Science and Technology, Pohang 790-784, Korea

[§]SKKU Advanced Institute of Nanotechnology (SAINT) and Center for Human Interface Nano Technology (HINT), Department of Chemistry, Sungkyunkwan University, Suwon 440-746, Korea

Supporting Information

ABSTRACT: Organic electronic devices that use graphene electrodes have received considerable attention because graphene is regarded as an ideal candidate electrode material. Transfer and lithographic processes during fabrication of patterned graphene electrodes typically leave polymer residues on the graphene surfaces. However, the impact of these residues on the organic semiconductor growth mechanism on graphene surface has not been reported yet. Here, we demonstrate that polymer residues remaining on graphene surfaces induce a stand-up orientation of pentacene, thereby controlling pentacene growth such that the molecular assembly is optimal for charge transport. Thus, pentacene field-effect transistors (FETs) using source/drain monolayer graphene electrodes with polymer residues show a high field-effect mobility of 1.2 cm^2/V s. In contrast, epitaxial growth of pentacene having molecular assembly of lying-down structure is facilitated by $\pi-\pi$ interaction between pentacene and the clean graphene electrode without polymer residues, which adversely affects lateral charge transport at the interface between electrode and channel. Our studies provide that the obtained high field-effect mobility in pentacene FETs using monolayer graphene electrodes arises from the extrinsic effects of polymer residues as well as the intrinsic characteristics of the highly conductive, ultrathin two-dimensional monolayer graphene electrodes.

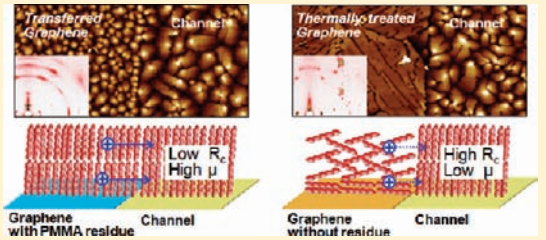

INTRODUCTION

Graphene, a two-dimensional allotrope of carbon with a planar honeycomb lattice, has attracted much attention due to its fascinating electrical and mechanical properties.[1−8] Among various graphene synthesis methods, chemical vapor deposition (CVD) is the most promising approaches because it provides large-scale production of graphene films with high electrical conductivity and field-effect mobility properties.[9−12] However, as-grown graphene films on metal substrates or foils, prepared by CVD, must be transferred to a target substrate and patterned by lithographic techniques to fabricate graphene-based electronic devices. During the transfer and patterning processes, impurities or polymer residues are inevitably physisorbed onto the graphene surfaces, so that the chemical and physical properties of the graphene are altered. Although graphene-based sensors utilize this demerit by measuring the electric current modulation due to physisorption,[13−15] the surface properties of graphene have largely been ignored in the context of graphene-based organic electronic device fabrication.

The high conductivity and transparency of graphene electrodes have been employed in organic field-effect transistors (OFETs) and organic photovoltaic solar cells.[16−22] However, the growth characteristics of organic semiconductors affected by the surface properties of graphene have not been fully examined. Without understanding their importance in the performance of organic electronic devices, only the conductivity properties of the used graphene have been discussed so far.[17,19,20,22] Although the growth characteristics of organic semiconductors on chemically driven graphene (i.e., reduced graphene oxide, RGO) have been studied,[18] the surface properties of RGO are totally different from those of pristine graphene (i.e., mechanically exfoliated graphene). It is shown that the reduction process cannot fully recover the surface properties of graphene after oxidation.[23,24]

Over the past several decades, the molecular arrangements of organic semiconductors on highly oriented pyrolytic graphite (HOPG) surfaces have been studied extensively.[25−29] Because most organic semiconductors consist of π-conjugated planar acenes, these molecules can interact with the underlying HOPG surface via $\pi-\pi$ interactions[30−32]and are arranged according to a quasi-epitaxial growth mode.[30] However, the uniform arrangement of organic semiconductors on HOPG surfaces is not easily obtained. Ordered monolayer or film growth is usually locally restricted to small surface areas, as HOPG surfaces include

Received: October 29, 2010
Published: March 07, 2011

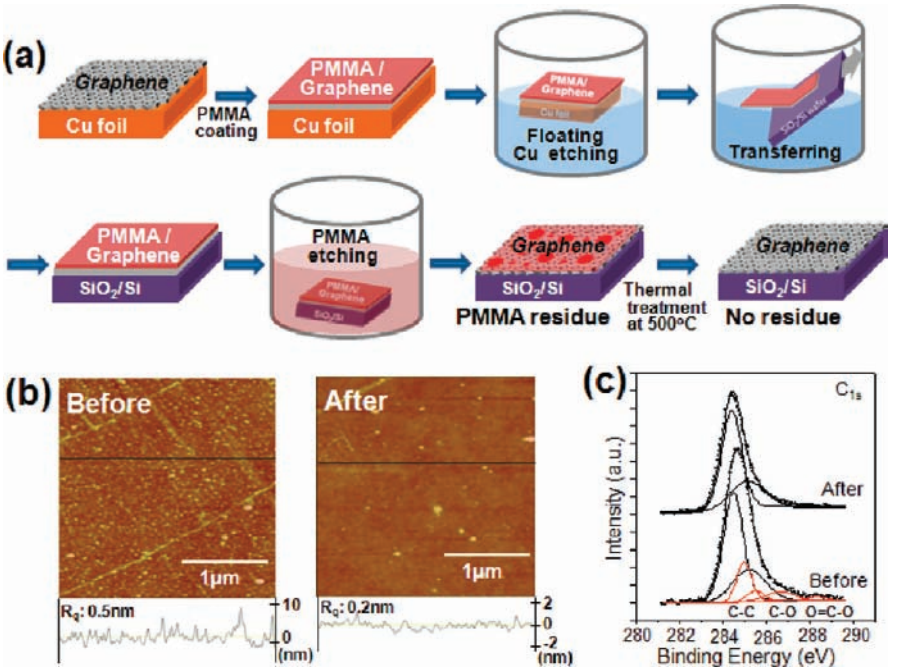

Figure 1. Schematic of the fabrication process for producing a monolayer graphene film on a target SiO_2/Si substrate (a). AFM images (height scale 20 nm) of graphene films before and after thermal treatment (b). XPS C_{1s} spectra of graphene films before and after thermal treatment (c). Before thermal treatment, typical peaks corresponding to four distinct components of PMMA and graphene were observed (red lines).

monatomic step edges and organic semiconductors do not grow across such step edges.[33] The molecular arrangement of perylene-3,4,9,10-tetracarboxylic dianhydride, a representative planar acene, on large-area epitaxial graphene grown on a SiC (0001) surface was recently studied by scanning tunneling microscopy (STM).[34] However, device applications that include epitaxial graphene and organic semiconductors grown on epitaxial graphene have scarcely been reported mainly because transferring in epitaxial graphene is not feasible yet.

We report here for the first time the growth characteristics of pentacene, a representative organic semiconductor used in OFETs, on large-area monolayer graphene films fabricated by CVD. We also describe high-performance OFET devices that use monolayer graphene source/drain electrodes. The surface properties of graphene films were examined before and after the transfer and patterning processes, and the molecular orientations of pentacene on graphene films with different surface properties were revealed by structural analysis. It is important to note that polymer residues on graphene surfaces significantly influenced the molecular orientations and, hence, the growth characteristics of pentacene, which in turn impacted the electrical properties of OFETs using graphene electrodes.

EXPERIMENTAL SECTION

Materials and Device Fabrication. Monolayer graphene films were prepared following the CVD process reported in the literature.[11,35] As-grown monolayer graphene films on a copper foil were covered with polymethylmethacrylate (PMMA, $M_w = 240$ kg mol^{-1}) and floated in an aqueous solution of 0.1 M ammonium persulfate [$(NH_2)_4S_2O_8$] solution. After all copper layers had been etched away, the graphene film with the PMMA support was transferred to a silicon substrate with a 300 nm SiO_2 layer (capacitance = 10.8 nF cm^{-2}). The graphene film remained on the silicon substrate after removing the PMMA support with acetone. E-beam lithography was used to pattern the graphene electrodes with defined channel lengths and widths ($L = 10, 20, 50, 100\ \mu$m; $W = 1000\ \mu$m). Etching of the graphene film was performed by application of a reactive ion etching (RIE) plasma (100 W, O_2 gas flow) for 2 s, and a lift-off technique was used to remove the PMMA. Thermal treatment of the sample at temperatures (~500 °C) was conducted to remove residual PMMA. Finally, pentacene (Aldrich Chemicals, no purification) was deposited from a quartz crucible onto the substrates (graphene films before or after thermal treatment) at a rate of 0.2 Å/s to construct the pentacene field-effect transistors with graphene source/drain electrodes.

Characterization. Thickness of pentacene films was determined by measuring nominal thickness using quartz crystal microbalance attached to the deposition chamber. The film morphologies were characterized by optical microscopy (Zeiss) and AFM (Digital Instruments Multimode). The UV−vis absorption and Raman spectra were obtained using a Varian Cary-5000 and CRM 200 spectrometer, respectively. Near-edge X-ray absorption fine structure (NEXAFS) and 2D grazing incidence diffraction (GIXD) experiments were performed at the 4B1 and 4C2 beamlines of the Pohang Accelerator Laboratory to study the molecular orientations in the pentacene films. The work function of the electrodes and the injection barrier between the electrodes and the pentacene were measured by depositing pentacene in several steps in an ultrahigh vacuum chamber (base pressure $<5 \times 10^{-10}$ Torr) on the graphene films before or after thermal treatment. At each step, the interface between the pentacene and graphene was characterized by measuring the secondary electron cutoff and valence band spectra by UPS at the 4B1 beamline of the Pohang Accelerator Laboratory. Keithley 2636A semiconductor parameter analyzer was employed to study the current−voltage characteristics of the devices.

RESULTS AND DISCUSSION

Figure 1a shows a schematic illustration of the fabrication steps for producing monolayer graphene on a SiO_2/Si substrate. An as-grown graphene film on a copper foil was covered with

dx.doi.org/10.1021/ja1097463 |J. Am. Chem. Soc. 2011, 133, 4447–4454

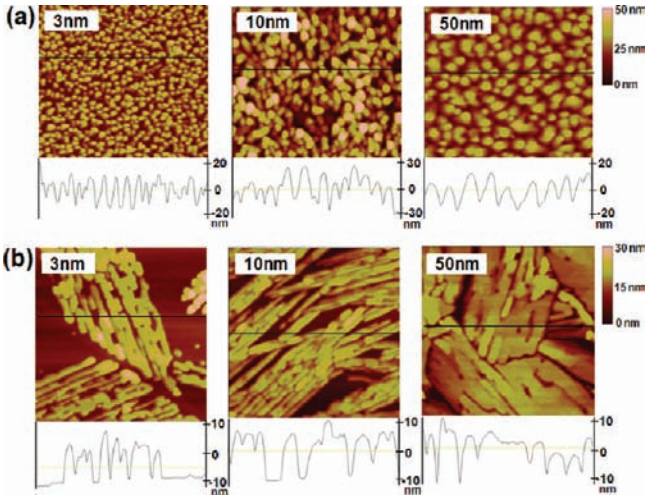

Figure 2. AFM images (2 × 2 μm) collected at various thicknesses during formation of the pentacene film on untreated graphene films (a) and thermally treated graphene films (b).

polymethylmethacrylate (PMMA) and floated in an aqueous solution of 0.1 M ammonium persulfate [$(NH_2)_4S_2O_8$]. After copper layers were etched away, the graphene film with PMMA support was transferred to a target substrate. The graphene film remained on the substrate after removal of the PMMA support with acetone. Preferential monolayer growth was confirmed by UV−vis spectroscopy and Raman spectroscopy (Figure S1, Supporting Information). The D-band peak was almost negligible, confirming the high quality of the graphene. However, PMMA residues were evident on the graphene film surfaces (Figure 1b, left). These residues remained, even after the solvent was substituted and the soaking time was increased. Thermal treatment of the sample at temperatures (~500 °C) to decompose any residual PMMA was found to be an effective way to remove these residues. After thermal treatment of the graphene film, the surface roughness decreased drastically, and a clean surface morphology was observed (Figure 1b, right). The X-ray photoelectron spectroscopy (XPS) spectra, shown in Figure 1c, revealed four distinct features corresponding to the structural elements of PMMA and graphene, which included C—O and O═C—O groups observed in the graphene films before thermal treatment.[36] On the other hand, only sp^2- and sp^3-hybridized states for the C_{1s} peak were observed after thermal treatment, showing that PMMA was effectively removed by thermal treatment of the graphene film at 500 °C. In addition to the disappearance of the four different PMMA features, the C1s peaks shifted to lower binding energies. The change in the peak position upon thermal treatment was due to structural distortion and p-doping of the graphene, as demonstrated in the Raman spectra (Figure S2, Supporting Information) and described in the literature.[37,38]

AFM images of the pentacene films, shown in Figure 2, revealed remarkably different pentacene growth characteristics, dependent on the surface properties of the graphene film. On a graphene film prior to thermal treatment (Figure 2a), many small nuclei were observed on a 3 nm thick pentacene film. Pentacene grains grew laterally and vertically as the thickness of the pentacene layer increased. Nucleation during pentacene film growth was most likely facilitated by the PMMA surface roughness, shown in Figure 1b, thereby increasing the pentacene nucleation density.

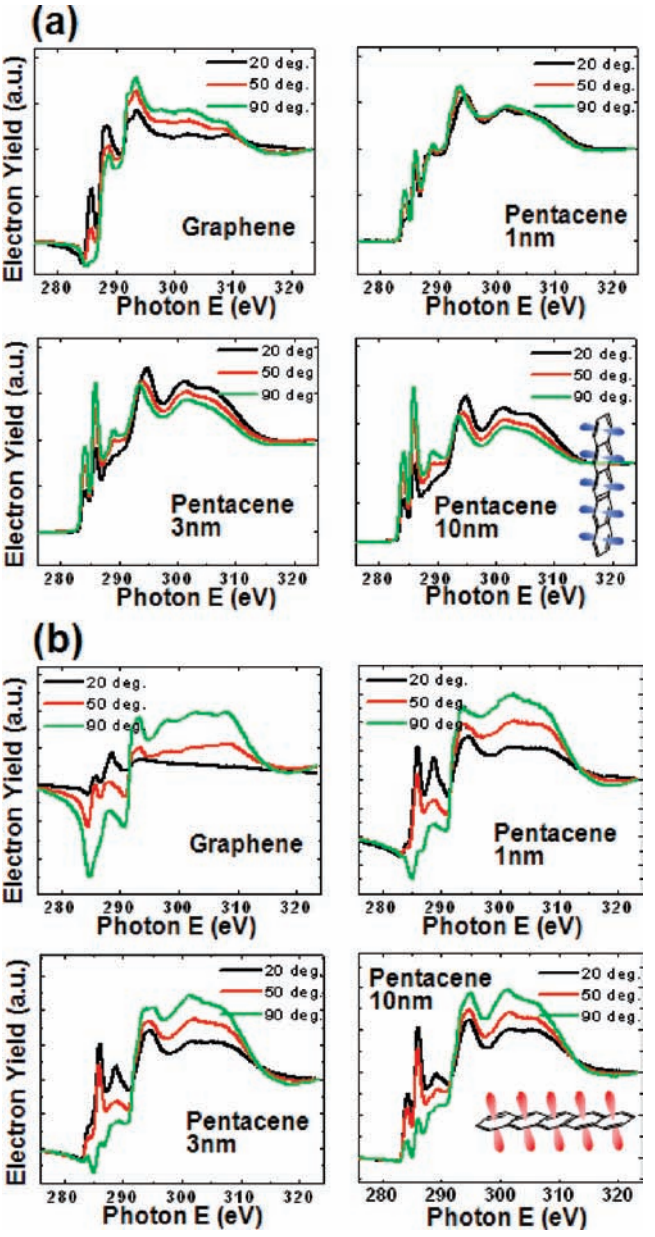

Figure 3. NEXAFS spectra of the pentacene films grown on the graphene films (0, 1, 3, and 10 nm thick pentacene films) before (a) and after (b) thermal treatment. The spectra were acquired at different photon incident angles (20, 50, and 90°). Insets show molecular structure of pentacene with the direction of π-orbitals.

The barrier height for heterogeneous nucleation is lowered by surface irregularities, while it is accelerated on rough surfaces.[39,40] In contrast, the graphene film after thermal treatment (Figure 2b) yielded pentacene films with a fiber-like texture that resembled the molecular arrangement of pentacene on highly oriented pyrolytic graphite (HOPG), as shown in Figure S3 of the Supporting Information and described in the literature.[41] Pentacene films with deep trenches and distinct angles are characteristic of the growth of highly oriented pentacene crystals that nucleated from the graphene lattice. The π-electrons in pentacene interacted with the graphene surface, and epitaxial growth was facilitated by these interactions.[30,42] These interactions were not present on the graphene films prior to thermal treatment, as the

dx.doi.org/10.1021/ja1097463 |J. Am. Chem. Soc. 2011, 133, 4447–4454

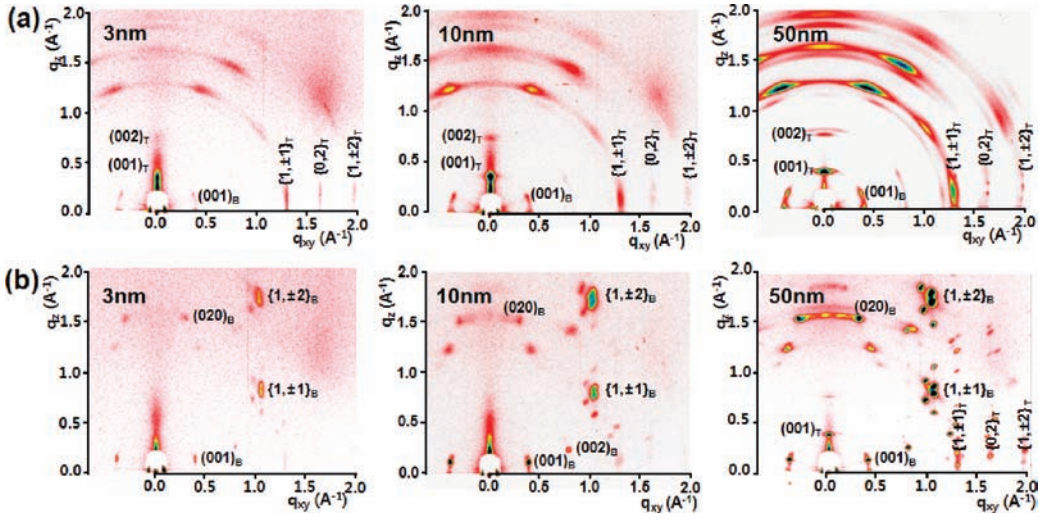

Figure 4. 2D GIXD patterns of the 3, 10, 50 nm thick pentacene films deposited on untreated graphene films (a) and thermally treated graphene films (b).

PMMA residues on the graphene surfaces reduced the strength of the pentacene−graphene interactions.

The two different growth characteristics of pentacene films, which are dependent on surface properties of graphene, were corroborated by angle-dependent near edge X-ray absorption fine structure (NEXAFS) measurements of graphene films and pentacene films grown on graphene films (Figure 3). Graphene, which is composed of extended sp^2-hybridized conjugated sheets, features a strong directionality in the orientations of the π and σ orbitals. The intensity of the peak at 285.7 eV, which originates from a $C_{1s} \rightarrow C{=}C\ \pi^*$ excitation, decreases as the incident angle increases. On the other hand, the intensities of peaks at 293.3 and 302.3 eV, which originate from a $C_{1s} \rightarrow C{-}C\ \sigma^*$ excitation and a $C_{1s} \rightarrow C{=}C\ \sigma^*$ excitation, respectively, increase as the incident angle increases (Figure 3a, graphene). These results indicate that the π orbitals are directed normal to the basal plane of the surface, whereas the σ orbitals lie along the basal plane. After thermal treatment of the graphene, the peak intensities and features persist, and the directionality increases slightly (Figure 3b, graphene).

When pentacene molecules are deposited onto a graphene film, the molecular orientations can vary significantly depending on whether the graphene film was thermally processed. On a graphene film not submitted to thermal treatment, pentacene molecules adopt a stand-up orientation, as indicated by the double peaks corresponding to $C_{1s} \rightarrow C{=}C\ \pi^*$ excitation (284.3, 285.9 eV), which are most intense at a 90° incident angle (Figure 3a), pentacene 3, 10 nm). On the other hand, a graphene film submitted to thermal treatment induces a lying-down molecular orientation for the pentacene molecules, as indicated by the peak corresponding to $C_{1s} \rightarrow C{=}C\ \sigma^*$ excitation (~301.3 eV), which is most intense at a 90° incident angle (Figure 3b, pentacene 1, 3, 10 nm). The angle-dependent NEXAFS spectra clearly demonstrated that pentacene molecules adopted a stand-up orientation on graphene films before thermal treatment and a lying-down orientation on graphene films after thermal treatment as schematically shown in the right/bottom insets of Figure 3a and b.

To further examine structural characteristics of pentacene films grown on two different graphene films, two-dimensional grazing incidence X-ray diffraction (2D GIXD) patterns were collected with varying pentacene thickness (Figure 4). A graphene film before thermal treatment (Figure 4a) displayed intense (001) crystalline reflections along the q_z direction (surface normal), which could be categorized as a "thin-film" crystalline phase. Furthermore, {1, ± 1}, {0, 2}, and {1, ± 2} "thin-film" crystalline reflections appeared vertically with respect to the given q_{xy} direction. These vertically aligned Bragg rod reflections indicated that the pentacene molecules adopted highly oriented multilayered structures with a (001) crystalline plane directed toward the surface normal.[43] Conversely, the (001) crystalline reflection along the q_{xy} direction was relatively weak, confirming a deficiency in the lying-down pentacene molecules. By contrast, films grown on thermally treated graphene (Figure 4b) yield intense (001) crystalline reflections tilted by 18° with respect to the q_{xy} direction, and these reflections were indistinct along the q_z direction. We note that these reflection spots coincided precisely with the lying-down molecular arrangement in the "bulk (or single-crystal)" phase pentacene structure described in the literature (a = 0.6266; b = 0.7775; c = 1.453; α = 76.475; β = 87.682; γ = 84.684).[44] This preference for the lying-down molecular arrangement in pentacene films has been reported for Ag (111) and Au (111) substrates as well.[45,46] A density functional theory simulation of pentacene monolayers on graphite surfaces predicted ABAB-type stacking in the graphene layers of graphite.[47] This result corresponds well with our experimentally observed lying-down molecular arrangement, as schematically shown in Figure 5b. In addition, the (020) reflection tilted by 12° with respect to the q_z direction, and the {1, ± 1} reflections azimuthally rotated by 40° from the (020) reflection were highly visible. The diffraction peaks agreed with a pentacene molecular stacking arrangement in the bulk phase in which the (020) plane was tilted by 12° with respect to the surface normal (Figure S4, Supporting Information).

We propose that pentacene molecules adopt a lying-down orientation if the graphene−pentacene interactions are relatively strong (in monolayer conditions). As the pentacene layer grows to a thickness of several molecules, atomically flat adsorption sites are no longer present, and subsequent pentacene molecules tend to tilt in a specific molecular orientation.[41,45] This mechanism was supported by the 2D-GIXD patterns of 10 and 50 nm thick pentacene films, which showed a gradual increase in the

dx.doi.org/10.1021/ja1097463 |J. Am. Chem. Soc. 2011, 133, 4447–4454

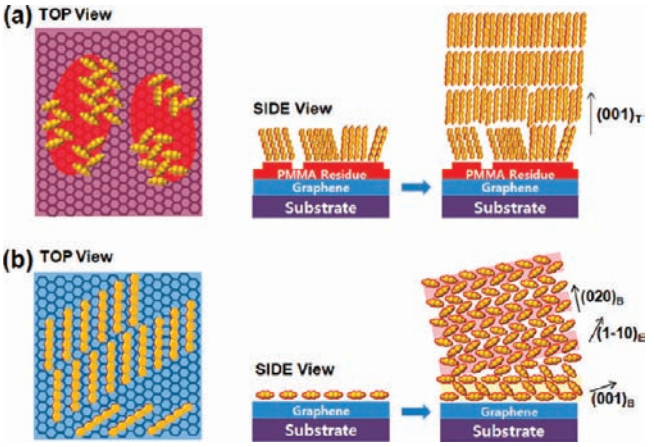

Figure 5. Schematic representations of the possible molecular packing orientations during growth of the pentacene film on untreated graphene films (a) and thermally treated graphene films (b).

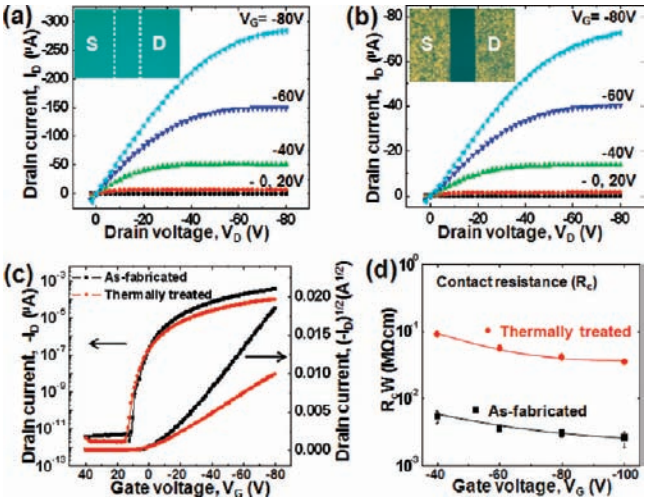

Figure 6. The output characteristics of FETs on untreated graphene electrodes (a) and thermally treated graphene electrodes (b). The inset shows OM images of channel regions, including electrodes (channel length = 100 μm, width = 1000 μm). Electrode−channel interfaces are represented by white dotted lines. The transfer characteristics of FETs fabricated using graphene electrodes either before or after thermal treatment (c). Channel width-normalized contact resistances of the graphene electrodes before and after thermal treatment (d).

stand-up molecular arrangements as film thickness increased (Figure 4 b). The graphene surface with PMMA residues displayed pentacene growth that was dominated by $\pi-\pi$ interactions between pentacene molecules rather than by pentacene−PMMA−graphene interactions. For this reason, pentacene growth is such that the (001) surface with the lowest surface energy is parallel to the substrate,[48,49] and this leads to a stand-up molecular arrangement, as shown in Figure 5a. To further clarify the origin of pentacene growth differences, pentacene was deposited on the as-grown graphene/copper foil and graphene/copper foil which had been submitted to PMMA coating/etching process (Supporting Information, Figure S5). Pentacene molecules adopt a stand-up orientation on graphene/copper foil with polymer residues. In contrast, epitaxial growth of pentacene having molecular assembly of lying-down structure is facilitated by $\pi-\pi$ interaction between pentacene and as-grown graphene/copper foil. Morphological and structural characteristics of the pentacene films confirm that pentacene growth is dominantly affected by PMMA residue covering graphene surface.

The merits of using CVD-grown monolayer graphene sheets include low sheet resistance (~0.5 kΩ/sq) and ease of patterning via standard lithographic techniques. E-beam lithography was used to define graphene source/drain electrodes on a silicon substrate with a 300 nm thick SiO_2 layer (see Experimental section for the detailed fabrication process). The substrate onto which graphene electrodes were patterned was thermally treated immediately after removing the patterned PMMA; this was done to observe the effects of pentacene film structural differences on the electrical properties of the OFETs. Figure 6a−d shows the electrical characteristics of pentacene FETs with monolayer graphene electrodes before and after thermal treatment. Output curves in Figure 6a and b shows the desirable linear and saturation regimes with different saturation current levels (~300 μA for graphene before thermal treatment and ~80 μA after thermal treatment). Detailed device performances were obtained from the transfer characteristics (Figure 6c). The field-effect mobilities were calculated from the transfer characteristics of 15−20 devices in the saturation regime. Devices based on monolayer graphene electrodes prior to thermal treatment exhibited an average field-effect mobility of 1.2 cm^2/V s, which was one of the highest mobilities measured for bottom-contact pentacene-based FETs. This value was much higher than mobilities of FETs based on CVD-grown graphene/Cu or reduced graphene oxide/Au bilayer electrodes in the literature.[16,18] Devices based on monolayer graphene electrodes after thermal treatment produced significantly lower field-effect mobilities, and the devices showed an average field-effect mobility of 0.4 $cm^2/(V\ s)$ with a comparable current on−off ratio of 10^8.

To investigate the origin of these variations in field-effect mobility, the contact resistance of each electrode was calculated using the transfer-line method with a varying channel length of 10−100 μm (channel width of 1000 μm, Figure S6 in Supporting Information).[50−52] The contact resistances (R_C) were extracted from the $L = 0$ intersection of the resistances at each gate voltage (V_G), as illustrated by the following equation:

$$R_{total} = R_C + \frac{L}{WC_i\mu_i}(V_G - V_{T,i}) = R_C + R_{ch}$$

where μ_i and $V_{T,i}$ are the intrinsic field-effect mobility and the threshold voltage, respectively. R_{Total} was obtained from the inverse slope of each $I-V$ curve in the linear regime. The channel width-normalized contact resistances (R_cW) of graphene electrodes prior to thermal treatment were lower than those of graphene electrodes after thermal treatment (Figure 6d). The pentacene molecular stacking arrangements on each graphene electrode appeared to be responsible for the differences in contact resistance. Once charge injection occurs at an electrode, the injected charge carriers cross the interface between electrode and channel.[53,54] Continuous pathways are observed if the molecular orientation of pentacene on the source electrode is the same as that of pentacene on the channel.[55−57] As the pentacene molecules of the channel adopted a stand-up orientation (Figure S7, Supporting Information), the graphene electrode before thermal treatment behaved better than the graphene electrode after thermal treatment, on which pentacene molecules adopted a lying-down orientation.

dx.doi.org/10.1021/ja1097463 |J. Am. Chem. Soc. 2011, 133, 4447–4454

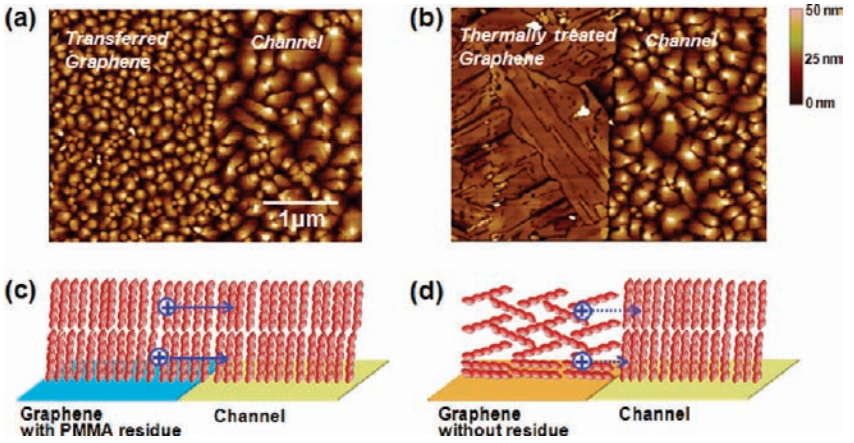

Figure 7. AFM images of the pentacene films (50 nm) near the interface between SiO_2 and untreated graphene electrodes (a) and thermally treated graphene electrodes (b). Schematic representations of the possible molecular packing orientations near the interface between SiO_2 and untreated graphene electrodes (c) and thermally treated graphene electrodes (d).

This explanation was further supported by OM and AFM of the interface between pentacene films on the channel region (SiO_2) as well as the graphene electrode (Figures 6a and b, insets, and 7). After thermal treatment, a morphological transition regime was clearly observed on graphene electrodes (Figures 6b, inset, Figure 7b). As the channel length decreased to 500 nm, the transition regime did not disappear, and the discontinuous morphology at the interface remained (Figure S8, Supporting Information). The observed transition regime introduced sites of large resistance for charge transport at the interface between an electrode and channel as schematically shown in Figure 7d. Conversely, films grown on graphene electrodes before thermal treatment displayed no discernible transition region, and continuous pentacene grain growth at the interface was observed (Figure 7a). For this reason, a low contact resistance and a high field-effect mobility were measured in a pentacene FET that used a graphene electrode with a PMMA residue, where efficient charge transport is facilitated at the interface between an electrode and a channel (Figure 7c). The PMMA residue covering the graphene surface is ultrathin with thickness of a few nanometers, and thus this thin PMMA layer does not increase contact resistance in bottom-contact FETs.[58]

To measure the work function of the graphene electrodes and the injection barrier between the electrodes and pentacene, ultraviolet photoemission spectra were obtained (Figure 8a and b). The work functions of the graphene before and after thermal treatment were calculated to be 4.6 and 4.75 eV, respectively. Thermal treatment at 500 °C activated the process of charge transfer, from graphene to the silicon substrate, which resulted in p-doping of the graphene and an increase in the graphene work function (Figure S2, Supporting Information). However, the hole injection barriers, which contribute to contact resistance, were found to be comparable, regardless of the thermal treatment of graphene (0.7 eV for the sample prior to thermal treatment and 0.6 eV after thermal treatment, Figure 8). These values were smaller than the hole injection barrier of commonly used Au electrodes,[59] and they remained within the limits of efficient hole injection. The hole injection barrier did not dominate the charge mobility properties. This explanation agrees with results presented in the recent paper of Asadi et al., in which the morphology of the interface between the electrode and the channel dominated the electrical properties of the OFET to a greater extent than manipulation of the hole injection barrier.[56]

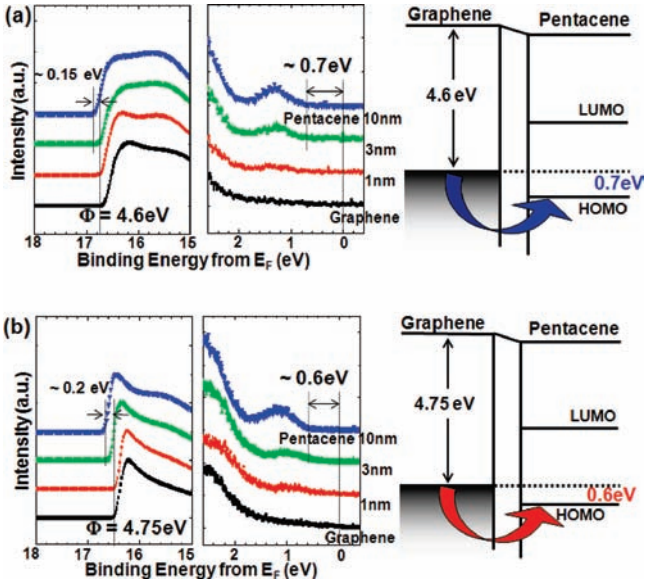

Figure 8. UPS spectra (left: secondary, right: highest occupied molecular orbital region) and schematic energy level diagram for pentacene on graphene before (a) and after (b) thermal treatment.

The outstanding performance, in terms of field-effect mobility (1.2 $cm^2/V\,s$) and on−off current ratio (in excess of 10^8), of our staggered bottom-contact OFETs has to be emphasized. Considering that no dielectric surface treatments or pentacene purification were applied, the FET performance is far more improved compared to other well-optimized top-contact OFETs. These properties resulted from the use of an ultrathin monolayer graphene electrode formed in the presence of a residual polymer film on the graphene surface. An one-atom-thick monolayer graphene electrode ensures excellent step coverage of the pentacene during sequential transistor fabrication. In addition, the residual polymer film induced a stand-up pentacene molecular orientation that enabled continuous pentacene growth through $\pi-\pi$ interactions at the interface between the electrode and the channel. This stand-up orientation in π stacks of pentacene molecules resulted in efficient charge transport through space between π stacks. This effect removed undesirable

dx.doi.org/10.1021/ja1097463 |J. Am. Chem. Soc. 2011, 133, 4447–4454

interactions between the graphene surface and the pentacene film, while benefiting from the properties of the highly conductive, ultrathin monolayer graphene. Our study showed that high-conductivity graphene electrodes must be combined with controlled molecular packing of organic semiconductors grown on the graphene surfaces, as this enhances the electrical properties of organic electronic devices based on graphene electrodes.

CONCLUSIONS

In summary, we have described the growth characteristics of pentacene films, which depend on the surface properties of graphene, in an effort toward fabricating high-performance OFETs. Polymer residues are inevitably physisorbed onto graphene surfaces during transfer and patterning processes. These residues induce a stand-up molecular orientation when growing a pentacene film. In contrast, clean graphene surfaces, from which polymer residues are removed by thermal treatment, are capable of π-interactions with pentacene that induce epitaxial pentacene growth to form pentacene crystals where molecules are arranged in a lying-down orientation. Interestingly, pentacene FETs using monolayer graphene source/drain electrodes with polymer residues exhibit an outstanding field-effect mobility of 1.2 cm^2/V s, which arise directly from continuous grain growth that benefits from identical molecular orientations of pentacene between channel and electrode. Our study reveals that polymer residues on graphene surfaces can be used to control the molecular orientations of organic semiconductor films grown on the graphene surfaces; this drastically enhances the performance of graphene-based electronic devices.

ASSOCIATED CONTENT

Supporting Information. Complete ref 12 and Figures S1−S8. This material is available free of charge via the Internet at http://pubs.acs.org.

AUTHOR INFORMATION

Corresponding Author

kwcho@postech.ac.kr; kim@postech.ac.kr; byunghee@skku.edu

Author Contributions

‖These authors contributed equally.

ACKNOWLEDGMENT

The authors would like to thank Dr. T.J. Shin and Dr. K. Ihm in the Pohang Accelerator Laboratory for GI-XD and NEXAFS measurements and discussions. This research was supported by a grant (F0004021-2010-33) from the Information Display R&D Center under the 21st Century Frontier R&D Program, the National Research Foundation (NRF) of Korea (No. 2009-0093485), NRF (National Honor Scientist Program: 2010-0020414), and Converging Research Center Program through the Ministry of Education, Science and Technology (2010K001066, 2009-0089030). The authors thank the Pohang Accelerator Laboratory for providing the synchrotron radiation sources at 4B1, 4C2, and 8A2 beamlines used in this study.

REFERENCES

(1) Geim, A. K.; Novoselov, K. S. *Nat. Mater.* **2007**, *6* (3), 183–191.
(2) Stankovich, S.; Dikin, D. A.; Dommett, G. H. B.; Kohlhaas, K. M.; Zimney, E. J.; Stach, E. A.; Piner, R. D.; Nguyen, S. T.; Ruoff, R. S. *Nature* **2006**, *442* (7100), 282–286.
(3) Zhang, Y. B.; Tan, Y. W.; Stormer, H. L.; Kim, P. *Nature* **2005**, *438* (7065), 201–204.
(4) Gilje, S.; Han, S.; Wang, M.; Wang, K. L.; Kaner, R. B. *Nano Lett.* **2007**, *7* (11), 3394–3398.
(5) Lee, C.; Wei, X. D.; Kysar, J. W.; Hone, J. *Science* **2008**, *321* (5887), 385–388.
(6) Eda, G.; Fanchini, G.; Chhowalla, M. *Nat. Nanotechnol.* **2008**, *3* (5), 270–274.
(7) Geim, A. K. *Science* **2009**, *324* (5934), 1530–1534.
(8) Rao, C. N. R.; Sood, A. K.; Subrahmanyam, K. S.; Govindaraj, A. *Angew. Chem., Int. Ed.* **2009**, *48* (42), 7752–7777.
(9) Reina, A.; Jia, X. T.; Ho, J.; Nezich, D.; Son, H. B.; Bulovic, V.; Dresselhaus, M. S.; Kong, J. *Nano Lett.* **2009**, *9* (1), 30–35.
(10) Kim, K. S.; Zhao, Y.; Jang, H.; Lee, S. Y.; Kim, J. M.; Kim, K. S.; Ahn, J. H.; Kim, P.; Choi, J. Y.; Hong, B. H. *Nature* **2009**, *457* (7230), 706–710.
(11) Li, X. S.; Cai, W. W.; An, J. H.; Kim, S.; Nah, J.; Yang, D. X.; Piner, R.; Velamakanni, A.; Jung, I.; Tutuc, E.; Banerjee, S. K.; Colombo, L.; Ruoff, R. S. *Science* **2009**, *324* (5932), 1312–1314.
(12) Bae, S.; et al. *Nat. Nanotechnol.* **2010**, *5* (8), 574–578.
(13) Schedin, F.; Geim, A. K.; Morozov, S. V.; Hill, E. W.; Blake, P.; Katsnelson, M. I.; Novoselov, K. S. *Nat. Mater.* **2007**, *6* (9), 652–655.
(14) Robinson, J. T.; Perkins, F. K.; Snow, E. S.; Wei, Z. Q.; Sheehan, P. E. *Nano Lett.* **2008**, *8* (10), 3137–3140.
(15) Dua, V.; Surwade, S. P.; Ammu, S.; Agnihotra, S. R.; Jain, S.; Roberts, K. E.; Park, S.; Ruoff, R. S.; Manohar, S. K. *Angew. Chem., Int. Ed.* **2010**, *49* (12), 2154–2157.
(16) Di, C. A.; Wei, D. C.; Yu, G.; Liu, Y. Q.; Guo, Y. L.; Zhu, D. B. *Adv. Mater.* **2008**, *20* (17), 3289.
(17) Pang, S. P.; Tsao, H. N.; Feng, X. L.; Mullen, K. *Adv. Mater.* **2009**, *21* (34), 3488.
(18) Lee, C. G.; Park, S.; Ruoff, R. S.; Dodabalapur, A. *Appl. Phys. Lett.* **2009**, *95* (2), 023304.
(19) Cao, Y.; Liu, S.; Shen, Q.; Yan, K.; Li, P. J.; Xu, J.; Yu, D. P.; Steigerwald, M. L.; Nuckolls, C.; Liu, Z. F.; Guo, X. F. *Adv. Funct. Mater.* **2009**, *19* (17), 2743–2748.
(20) Liu, W.; Jackson, B. L.; Zhu, J.; Miao, C. Q.; Chung, C. H.; Park, Y. J.; Sun, K.; Woo, J.; Xie, Y. H. *ACS Nano* **2010**, *4* (7), 3927–3932.
(21) Wang, Y.; Chen, X. H.; Zhong, Y. L.; Zhu, F. R.; Loh, K. P. *Appl. Phys. Lett.* **2009**, *95* (6), 063302.
(22) De Arco, L. G.; Zhang, Y.; Schlenker, C. W.; Ryu, K.; Thompson, M. E.; Zhou, C. W. *ACS Nano* **2010**, *4* (5), 2865–2873.
(23) Loh, K. P.; Bao, Q. L.; Ang, P. K.; Yang, J. X. *J. Mater. Chem.* **2010**, *20* (12), 2277–2289.
(24) Eda, G.; Chhowalla, M. *Adv. Mater.* **2010**, *22* (22), 2392–2415.
(25) Hoshino, A.; Isoda, S.; Kurata, H.; Kobayashi, T. J. *J. Appl. Phys.* **1994**, *76*, 4113–4120.
(26) Burrows, P. E.; Zhang, Y. E.; Haskal, I.; Forrest, S. R. *Appl. Phys. Lett.* **1994**, *61*, 2417–2419.
(27) Forrest, S. R.; Zhang, Y. *Phys. Rev. B: Condens. Matter Mater. Phys.* **1994**, *49*, 11297–11308.
(28) Chen, W.; Huang, H.; Thye, A.; Wee, S. *Chem. Commun.* **2008**, *36*, 4276–4278.
(29) Bussolotti, F.; Han, S. W.; Honda, Y.; Friedlein, R. *Phys. Rev. B: Condens. Matter Mater. Phys.* **2009**, *79* (24), 245410.
(30) Forrest, S. R. *Chem. Rev.* **1997**, *97* (6), 1793–1896.
(31) Lee, E. C.; Kim, D.; Jurecka, P.; Tarakeshwar, P.; Hobza, P.; Kim, K. S. *J. Phys. Chem. A* **2007**, *111* (18), 3446–3457.
(32) Kim, K. S.; Tarakeshwar, P.; Lee, J. Y. *Chem. Rev.* **2000**, *100* (11), 4145–4185.
(33) Huang, H.; Chen, S.; Gao, X. Y.; Chen, W.; Wee, A. T. S. *ACS Nano* **2009**, *3* (11), 3431–3436.
(34) Wang, Q. H.; Hersam, M. C. *Nat. Chem.* **2009**, *1* (3), 206–211.
(35) Lee, Y.; Bae, S.; Jang, H.; Jang, S.; Zhu, S. E.; Sim, S. H.; Song, Y. I.; Hong, B. H.; Ahn, J. H. *Nano Lett.* **2010**, *10* (2), 490–493.
(36) Ben Amor, S.; Baud, G.; Jacquet, M.; Nanse, G.; Fioux, P.; Nardin, M. *Appl. Surf. Sci.* **2000**, *153* (2−3), 172–183.

(37) Nourbakhsh, A.; Cantoro, M.; Klekachev, A.; Clemente, F.; Soree, B.; van der Veen, M. H.; Vosch, T.; Stesmans, A.; Sels, B.; De Gendt, S. *J. Phys. Chem. C* **2010**, *114* (15), 6894–6900.
(38) Ryu, S.; Liu, L.; Berciaud, S.; Yu, Y.; Liu, H.; Kim, P.; Flynn, G. W.; Brus, L. E. *Nano Lett.* **2010**, *10*, 4944.
(39) Venables, J. A.; Spiller, G. D. T.; Hanbucken, M. *Rep. Prog. Phys.* **1984**, *47*, 399.
(40) Mannsfeld, S. C. B.; Briseno, A. L.; Liu, S.; Reese, C.; Roberts, M. E.; Bao, Z. *Adv. Funct. Mater.* **2007**, *17* (17), 3545–3553.
(41) Koch, N.; Vollmer, A.; Salzmann, I.; Nickel, B.; Weiss, H.; Rabe, J. P. *Phys. Rev. Lett.* **2006**, *96* (15), 156803.
(42) Harada, Y.; Ozaki, H.; Ohno, K. *Phys. Rev. Lett.* **1984**, *52*, 2269–2272.
(43) Kim, D. H.; Lee, H. S.; Yang, H. C.; Yang, L.; Cho, K. *Adv. Funct. Mater.* **2008**, *18* (9), 1363–1370.
(44) Mattheus, C. C.; Dros, A. B.; Baas, J.; Meetsma, A.; de Boer, J. L.; Palstra, T. T. M. *Acta Crystallogr., Sect. C: Cryst. Struct. Commun.* **2001**, *57*, 939–941.
(45) Casalis, L.; Danisman, M. F.; Nickel, B.; Bracco, G.; Toccoli, T.; Iannotta, S.; Scoles, G. *Phys. Rev. Lett.* **2003**, *90* (20), 206101.
(46) Kafer, D.; Ruppel, L.; Witte, G. *Phys. Rev. B: Condens. Matter Mater. Phys.* **2007**, *75* (8), 85309.
(47) Paramonov, P. B.; Coropceanu, V.; Bredas, J. L. *Phys. Rev. B* **2008**, *78* (4), 041403.
(48) Northrup, J. E.; Tiago, M. L.; Louie, S. G. *Phys. Rev. B: Condens. Matter Mater. Phys.* **2002**, *66*, (12), XX−XX.
(49) Verlaak, S.; Steudel, S.; Heremans, P.; Janssen, D.; Deleuze, M. S. *Phys. Rev. B: Condens. Matter Mater. Phys.* **2003**, *68* (19), 195409.
(50) Cho, J. H.; Kim, D. H.; Jang, Y.; Lee, W. H.; Ihm, K.; Han, J. H.; Chung, S.; Cho, K. *Appl. Phys. Lett.* **2006**, *89* (13), 132101.
(51) Luan, S.; Neudeck, G. W. *J. Appl. Phys.* **1992**, *72*, 766.
(52) Lim, J. A.; Cho, J. H.; Park, Y. D.; Kim, D. H.; Hwang, M.; Cho, K. *Appl. Phys. Lett.* **2006**, *88* (8), 082102.
(53) Park, Y. D.; Lim, J. A.; Lee, H. S.; Cho, K. *Mater. Today* **2007**, *10* (3), 46–54.
(54) Di, C. A.; Liu, Y. Q.; Yu, G.; Zhu, D. B. *Acc. Chem. Res.* **2009**, *42* (10), 1573–1583.
(55) Dimitrakopoulos, C. D.; Malenfant, P. R. L. *Adv. Mater.* **2002**, *14* (2), 99–117.
(56) Asadi, K.; Wu, Y.; Gholamrezaie, F.; Rudolf, P.; Blom, P. W. M. *Adv. Mater.* **2009**, *21* (41), 4109.
(57) Dholakia, G. R.; Meyyappan, M.; Facchetti, A.; Marks, T. J. *Nano Lett.* **2006**, *6* (11), 2447–2455.
(58) De Angelis, F.; Cipolloni, S.; Mariucci, L.; Fortunato, G. *Appl. Phys. Lett.* **2005**, *86* (20), 203505.
(59) Koch, N.; Kahn, A.; Ghijsen, J.; Pireaux, J. J.; Schwartz, J.; Johnson, R. L.; Elschner, A. *Appl. Phys. Lett.* **2003**, *82* (1), 70–72.